Journal of Materials Chemistry A

Accepted Manuscript

ROYAL SOCIETY OF CHEMISTRY

www.rsc.org/materialsA

Journal of Materials Chemistry A

Cite this: DOI: 10.1039/c0xx00000x

www.rsc.org/xxxxxx

Full Paper

Naturally Derived Porous Carbon with Selective Metal- and/or Nitrogen- Doping for Efficient CO_2 Capture and Oxygen Reduction

Bingjun Zhu,[a] Kaipei Qiu,[a] Congxiao Shang,[b] and Zhengxiao Guo[a]*

Received (in XXX, XXX) Xth XXXXXXXXX 20XX, Accepted Xth XXXXXXXXX 20XX

DOI: 10.1039/b000000x

A heterogeneously porous "green carbon" structure was derived from abundant London Plane leaves and shows excellent performance for both CO_2 capture and Oxygen Reduction Reaction (ORR). The carbonised and KOH-activated carbon possesses a high level of micropores, a specific surface area exceeding 2000 m^2/g and a large pore volume over 1 cm^3/g, leading to an excellent CO_2 uptake of 19.4 wt% under ambient conditions and fast four-electron transfer in an alkaline medium for ORR. Further XPS and X-Ray analyses reveal well-dispersed metal elements (such as Mg and Ca) in the porous carbon, which are naturally doped and inherited from the leaf structure**,** and can help to enhance CO_2 adsorption. On the other hand, such metal elements do not positively affect catalytic performance in ORR. Hence, a purpose-specific cleaning approach after KOH activation, i.e. by water or acid, has been devised to obtain optimal functionalities for CO_2 capture or ORR.

Introduction

Mitigation of global climate change to reduce atmospheric CO_2 concentration includes two major approaches: carbon capture and storage (CCS) for fossil-fuel powered plants and deployment of renewable energy sources such as wind and solar. In both cases, the development of a highly efficient energy storage technology is important to increase grid efficiency and/or integrate renewables to the electrical grid. Porous carbon has long been regarded as an ideal CO_2 sorbent and an electrode material for energy conversion and storage devices, due to its relatively low cost, facile mass production and good stability under moisture, basic and acidic environments. More specifically, porous carbon features low energy consumption for material regeneration with regard to CO_2 capture, since gas molecules can be readily removed after adsorption due to the physisorption nature of carbon.[1, 2] It also shows high electrical conductivity as an electrocatalyst or electrode for fast electron transfer and large surface area to ensure sufficient active sites exposure.[3-5] In order to achieve optimised performance for both applications, carbon materials need to be further activated to generate microporous structures with high specific surface area. This is usually achieved by high temperature treatment with KOH. In addition, the performance of carbon materials can be further modified by various dopants, including both non-metallic (such as nitrogen or boron) and metallic (such as iron or cobalt) elements.[6-9] Typically, nitrogen functional groups at carbon edges can enhance CO_2 capture due to their Lewis basicity; the charge and spin re-distribution derived from nitrogen incorporation into carbon matrix can also facilitate the oxygen adsorption and dissociation during oxygen reduction reaction.[6] For metal doping, several studies have illustrated exceptional electrochemical performance from strongly coupled organic/inorganic hybrids.[10-12] However, the role of atomic metal doping for carbon capture has not been clearly investigated, particularly by experiment, though some computational simulations point to the importance of metallic doping.[13, 14]

Biomass is a renewable and competitive carbon precursor, compared with many others (such as polymers[15, 16]), because of its abundant reserve, low-cost and simple mass production. In contrast, the synthesis of polymeric precursors usually involves complex procedures and strict control of synthesis conditions. With regards to CO_2 capture, starch, cellulose and sawdust-derived carbon sorbents are prepared through KOH activation and reported to have CO_2 uptakes of 15.2, 15.5 and 21.2 wt% under 1 bar CO_2 and 25 °C, respectively.[17] With the KOH/carbon weight ratio 4:1 and activation temperature 800 °C, Wang et al. report their studies on celtuce derived porous carbon.[18] Their sample exhibits a CO_2 uptake of 19.2 wt% under the same test conditions. As for catalytic oxygen reduction, Gao et al. demonstrate that the nitrogen-doped carbon materials synthesised via hydrothermal treatment of *Gastrodia elata* followed by ionothermal pyrolysis exhibited excellent electrocatalytic activity for ORR with a dominant four-electron pathway in an alkaline medium.[19] Similarly, Zhu et al. select an abundant microorganism, *Bacillus subtilis*, as a carbon precursor.[20] Ionothermal treatment is adopted for carbonisation followed by acid activation, and the sample after base washing exhibits both excellent ORR electrocatalytic activity and superior performance as supercapacitors. These

earlier reports show superb potential of biomass derived carbon. Moreover, biomass-derived carbons also offer a favourable route for the study of beneficial effects of nitrogen doping and especially atomic metal doping, as metal-centres in biomass derivation of carbons are often a desirable isolated atomic sites. Such issues have not been clarified and discussed previously.

Herein, we present a facile synthesis of highly microporous carbon materials with a large surface area (> 2000 m^2/g) and pore volume over 1 cm^3/g via direct carbonisation of London plane leaves followed by KOH activation. Naturally occurring nitrogen and metal elements are preserved as dopants to enhance molecular sorption, e.g. for CO_2 capture. London Plane accounts for 50% of all planted trees in the urban area of London,[21] and thus generates a substantial amount of leaf wastes. This natural biomass material can be a potential "zero-cost" carbon precursor, which offers a "green material" to produce porous carbon materials and dispose this major urban waste. Besides, we demonstrate that the obtained nitrogen and/or metal-doped porous carbon could be selectively used as efficient CO_2 sorbents and ORR electrocatalysts. In particular, the role of metal doping in both applications is effectively studied. The results show that a small amount of Mg and Ca elemental dopants could effectively improve CO_2 sorption; nonetheless, these metals are identified as 'dead mass' for catalytic ORR activity. After removal of metals, the pure nitrogen-doped carbon materials show much improved electrochemical performance. In summary, our work show that the London Plane leaf wastes derived porous carbon is a promising low-cost, highly efficient and multi-functional "green" candidate for both CO_2 capture and energy storage applications.

Experimental Section

Sample Preparation

Fallen leaves from London Plane (*platanus* × *hispanica*) were collected from Gordon Square Garden near University College London's Bloomsbury Campus in July 2013. The leaves were washed to remove dust and dirt. The cleaned leaves were dried in a vacuum oven at 80 °C overnight. The dried leaves became crispy and were ground into small pieces by pestle and mortar. The ground leaves were carbonised at 600 °C for an hour in a horizontal tube furnace (VTF 15/75/450, Lenton, UK) with constant nitrogen gas flow. The corresponding ramping rate was 3 °C/min. After carbonisation, the resulting carbon was mixed with potassium hydroxide (Fisher Scientific, UK) in the KOH/carbon weight ratios of 1:1, 2:1 and 3:1 in 10 ml distilled water. The mixture was ultrasonically agitated for 30 mins to achieve a uniform suspension in the KOH solution. The solution was then dried to a solid mixture of KOH and carbon in a vacuum oven at 80 °C. The solid mixture was thermally activated at 600, 700 and 800 °C in the furnace, respectively, with the constant nitrogen flow for an hour. The corresponding ramping rate remained at 3 °C/min. The resulting carbon samples were washed repeatedly with distilled water until their pH values are neutral. In addition, another 700 °C treated sample was washed with 1M HCl acid to remove metal elements within. At the end, the samples were dried in the vacuum oven at 80 °C overnight. The samples are marked as LCx-y, where LC stands for leaf-derived carbon, x:1 is the weight ratio of KOH/carbon and y is the thermal treatment temperature. The HCl acid washed sample was marked as LC2-700H.

Characterisations

Sample morphologies were captured by a field-emission scanning electron microscope (SEM, JSM 6301F, JEOL, Japan). In addition, a transmission electron microscope (TEM, JEOL 2100, Japan) was used to obtain the high resolution images of carbon structures. An X-ray photoelectron spectrometer (XPS, K-ALPHA, Thermo Scientific, USA) was employed to analyse the chemical composition of the samples. The identities of elements and chemical compounds were retrieved from the NIST XPS online database by searching their corresponding binding energies in the database system.[22] An X-ray diffractometer (XRD, Stadi P, STOE, Germany) was used to detect the existence of any crystals of metal or metal compounds in the samples. The porosities of the samples were analysed by an automated gas sorption analyser (Autosorb-iQ C, Quantachrome, USA). The specific surface area, specific micropore surface area, micropore volume and pore size distribution were derived from its corresponding nitrogen sorption isotherm at -196 °C (liquid nitrogen) and calculated by the Non-Local Density Functional Theory (slit/cylindrical pores) equilibrium model (NLDFT). The total pore volume was derived from the amount gas adsorbed at the partial pressure $P/P_0 = 0.99$. The same gas sorption analyser was also used to measure CO_2 adsorption capacities from 0.01 to 1 bar at 0 and 25 °C. In addition, the ultramicropore volume (pore size<0.7 nm) was derived from the 0 °C CO_2 isotherm and calculated by the "CO_2 on carbon at 273 K NLDFT" model. The heat of adsorption was calculated by the Clausus-Clapeyron Equation based on the CO_2 adsorption isotherms at 0, 25 and 50 °C.

Electrochemical Measurement

Cyclic and rotating voltammetry were measured in O_2-saturated 0.1M KOH. For electrode preparation, 4 mg catalyst was added in a mixture of 100 µl nafion (5 wt% in alcohol and water, Sigma-Aldrich) and 900 µl distilled water, followed by one-hour sonication so as to achieve uniform dispersion of the sample in the solvent. 5 µl catalyst suspensions were then drop casted on a glassy carbon (GC) working electrode (3mm diameter, Metrohm) and dried at 60 °C. The ORR activity was tested in a three-electrode configuration. Ag/AgCl (sat. KCl, Sigma-Aldrich) was used as a reference electrode and platinum sheet (Metrohm) was used as the counter electrode. Oxygen was purged into electrolyte for an hour before measurement and kept bubbling during the tests, in order to make sure the electrolyte oxygen saturated. The scan rate for cyclic and rotating voltammetry was 100 and 10 mV/s, respectively. All the results were recorded by a Metrohm Autolab 302N.

Results and Discussion

Morphologies of Leaf and Leaf-derived Carbon

The freshly collected London plane leaves are bright green due to

the existence of chlorophyll. However, the leaves became yellow and crispy after being dried in a vacuum oven. The dehydration converts chlorophyll into pheophytin.[23] With decreasing chlorophyll content, the orange, yellow, brown and grey colours of carotenoid and pheophytin pigments emerge. After carbonisation, the leaves turn into black carbon.[24]

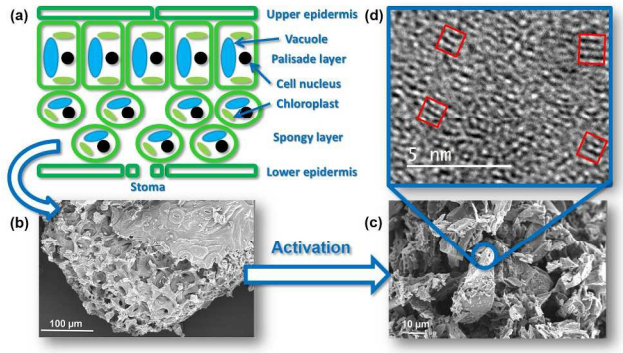

Figure 1 Illustration of leaf structure and its morphology and porous structure after chemical activation: (a) Schematic of a leaf cellular structure; (b) SEM image of a carbonised leaf; (c) Porous carbon fragments after KOH activation and (d) TEM image indicating nano-platelets within an amorphous carbon matrix after chemical activation. Examples of nano-platelets are indicated by the red squares.

Figure 1 shows the morphological change from a leaf to a porous carbon structure. The macroporous sponge layer beneath the cuticle layer of the dried leaf is clearly exposed in the SEM image, Figure 1(b). Several stomata on the cuticle suggest that it is the lower epidermis side of the leaf and thus the macroporous sponge layer can be observed beneath the epidermis. This macroporous structure of the sponge layer is retained even after carbonisation at 600 °C. Such well-preserved interconnected macroporous structure facilitates the impregnation of the carbonised sample by the KOH solution for rapid and uniform activation. The activated sample shows disintegrated porous carbon fragments of micrometre sizes. The corresponding high resolution TEM image (Figure 1d) reveals randomly oriented graphitic nano-platelets (as indicated by the red squares). The image shows that the nanoporous carbon structure consists of defective graphitic nano-platelets embedded in an otherwise amorphous carbon matrix. As a result, the discontinuity in the carbon nanostructure leads to the formation of a large number of voids. These voids are the origin of micropores, which contribute to the large specific surface area and pore volume in the resulting samples.

Porous Structure of Leaf-Derived Carbon

The porosity characteristics of the derived carbon sorbents are summarised in Table 1, including cumulative specific surface area (S_{N2}), specific micropore surface area (S_{Micro}), total pore volume (V_{N2}), micropore volume (V_{Micro}) and ultramicropore volume (V_{CO2}, <0.7 nm).

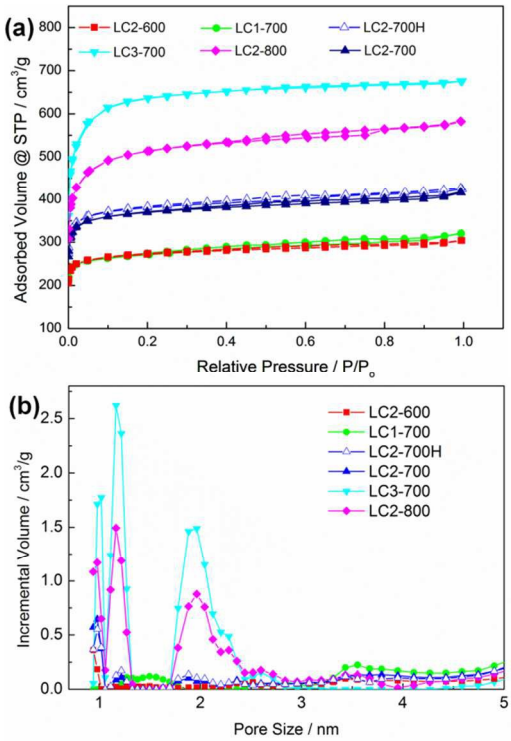

Figure 2 (a) N_2 sorption isotherms at -196 °C and (b) corresponding pore size distributions of leaf-derived carbon sorbents.

Table 1 Porosity characteristics of leaf-derived carbon sorbents.

Method	N_2 sorption				CO_2 sorption
Sample	S_{N2} /m²/g	S_{Micro} /m²/g	V_{N2} / cm³/g	V_{Micro} / cm³/g	V_{CO2}/ cm³/g
LC2-600	1210	1160	0.48	0.39	0.27
LC1-700	1360	1300	0.51	0.40	0.29
LC2-700	1600	1550	0.65	0.54	0.30
LC2-700H	1630	1580	0.66	0.56	0.31
LC3-700	2230	2130	1.03	0.89	0.28
LC2-800	1950	1810	0.88	0.72	0.32

Figure 2a shows that all N_2 isotherms exhibit typical features of the Type–I sorption isotherm, which suggests that the sorbents mainly consist of micropores. This is reflected in Figure 2b that all sorbents show three major peaks in the micropore size regime (<2 nm) at 1, 1.2 and 2 nm, respectively. Table 1 shows the structural characteristics of carbon sorbents prepared with different weight ratios of KOH/carbon and activation temperatures. It can be concluded that the specific surface area and pore volume increase with the KOH/carbon weight ratio and activation temperature. The sample LC3-700 prepared with KOH/carbon = 3:1 and at 700 °C presents the highest specific surface area of 2230 m^2/g and pore volume of 1.03 cm^3/g. However, when it comes to ultramicropore volumes (V_{CO2}, <0.7 nm), LC2-800 shows the highest values. At lower KOH/carbon weight ratios and activation temperatures, the ultra-micropores are less well developed. The accumulation of KOH in localised area on the sample surface may result in reduced micropores due to excessive reactions between KOH and carbon. It has been well-discussed in the literature that KOH activation reaction is significantly influenced by the KOH/carbon weight ratio and activation temperature.[25-27] The chemical activation reaction removes carbon atoms from the carbon structure to create porosity. Below 700 °C, the activation reaction mainly produces potassium oxides and potassium carbonates with CO_2, H_2, CO and H_2O as the main gaseous products. The removal of carbon atoms is mainly carried out of by the gasification reaction between carbon and H_2O, where H_2O is generated from the dehydration reaction of KOH. Above 700 °C, potassium carbonate further decomposes into potassium oxide and carbon dioxide; and carbon reduces carbon dioxide, potassium carbonate and potassium oxide into carbon monoxide and elemental potassium, respectively.[25-27] These additional carbon removal reactions raise the level of activation, either by creating more micropores or enlarging the sizes of existing pores. It is also important to note that the N_2 sorption isotherm of LC2-700H is at a similar position to LC2-700. In addition, LC2-700H shows a higher ultramicropore volume, which can be attributed to the acid-washing process.

Chemical Analysis on Leaf-derived Carbon

The surface chemical composition of all samples were characterised by XPS and the results are summarised in Table 2. The analyser only detects carbon, oxygen and minor nitrogen in leaves without other anticipated elements, such as metallic elements. The reason is that a piece of leaf is protected by both upper and lower cuticles, which comprise of layers of waxes and dead cells with only cell walls but without the other living cell components, such as cytoplasm and nucleus.[28] The major components in cell walls are cellulose, hemicellulose and lignin, which mainly contain carbon and oxygen elements. The thickness of a cuticle layer can vary from 0.1 to 10 μm,[29] far beyond the detection limit of XPS analysis (1 to 10 nm).[30] Therefore, it cannot acquire the chemical information below both upper and lower cuticle layers. Even if some parts of the mesophyll layer are exposed (Figure 1), the thickness of the cell wall can vary from 0.1 to 10 μm as well,[31] which is still too thick for XPS analysis. In addition, within the original leaf, the levels of carbon and oxygen are much higher than the other elements. Therefore, their high peak intensities suppress peaks of other elements in this case. After losing certain amount of carbon and oxygen, due to carbonisation and activation, it reveals more elements, such as potassium, magnesium, calcium, sodium, phosphate and chlorine. It also detects a higher level of nitrogen in the other samples after activation, thanks to the etching of cell walls, which exposes more intracellular nitrogen-containing compounds. The existence of these elements is anticipated because all of those are the essential elements in various nutrients for plants. Nitrogenous, phosphatic and potassic fertilisers are the three most used nutrients in agriculture. They are the key ingredients in various plant cell components, such as amino-acids and chlorophylls, catalysts for synthesis reactions and activators for enzymes.[24] Metal-containing nutrients may be fertilised in the form of their corresponding chlorides due to their high solubility in water. This can explain the existence of chlorine in Table 2.

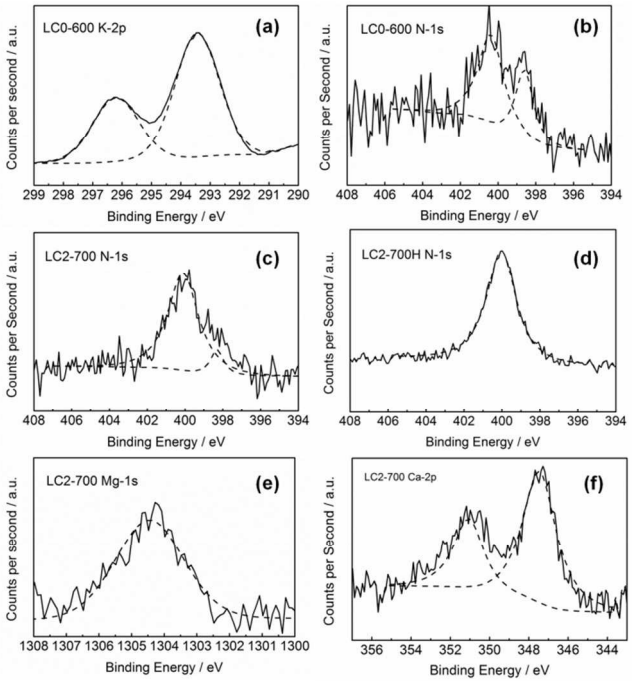

Figure 3 High resolution XPS spectra of major chemical elements in leaf-derived carbon.

Potassium and sodium are important chemical components in plant cells. During carbonisation, organic cell membranes decompose at the high temperature and thus it releases the potassium and sodium contents in cytoplasm. As a result, these two elements can be detected after carbonisation. Figure 3a and S1 are the high resolution XPS K-2p and Na-1s spectra of the carbonised sample LC0-600. The K-2p spectrum shows two peaks at 296.3 and 293.4 eV, which correspond to the binding energies of K-2p1/2 and K-2p3/2 electrons, respectively. The sodium spectrum shows a weak peak at 1071.9 eV, which corresponds to the binding energy of Na-1s electrons.

Nitrogen is another element that emerges after carbonisation. It is usually assimilated by plants in the form of nitrates, nitrites and ammonium salts and transformed into proteins, chlorophylls, nucleus acids and other active components in plant cells.[24] These nitrogen-containing substances cannot survive high temperature

treatments. However, an earlier study has shown intracellular amino acids and proteins can react with pectin during the pyrolysis and thus this reaction fixes nitrogen in the resulting carbon.[32] Overall, only 0.9 at% nitrogen is found at the surface of the carbonised sample LC0-600, since those nitrogen-containing substances are not intrinsic in the lignocellulosic compounds in cell walls and most of the nitrogen may be lost due to the high temperature treatment.

Table 2 Chemical composition analysis of original, carbonised and activated leaves.

Sample	Chemical composition (at%)								
	C	O	N	K	Mg	Ca	Na	P	Cl
Leaf	92.2	7.6	0.2	0	0	0	0	0	0
LC0-600	56.4	29.0	0.9	12.3	0	0	0.4	0	1.0
LC1-700	81.3	15.3	1.0	0	0.3	1.7	0	0.4	0
LC2-700	84.4	12.6	1.3	0	0.3	1.1	0	0.30	0
LC2-700H	85.5	12.0	2.5	0	0	0	0	0	0
LC3-700	86.5	11.9	0.4	0	0.3	0.9	0	0.01	0
LC2-600	78.6	17.6	1.7	0	0.2	1.2	0	0.7	0
LC2-800	84.8	11.9	0.4	0	0.9	1.6	0	0.4	0

The amount of nitrogen detected by XPS in the activated carbon samples is also influenced by the cell structure. Though it has been reported in the literature that nitrogen content in carbon is significantly reduced after chemical activation,[15] the 700 °C activated sample LC2-700 shows 1.3 at% nitrogen, which is even slightly higher than that in LC0-600 (0.9 at%). The same observation can be applied to LC2-600 and LC1-700. This phenomenon can be explained by the etching of cell walls and the expose of more nitrogen-containing compounds. There is severe loss of nitrogen in LC2-800 and LC3-700 due to more aggressive KOH activation.

Although the level of nitrogen is increased in LC2-700, the composition of different forms of nitrogen is still consistent with the earlier studies. Figure 3b, c and d are the high resolution N-1s spectra of LC0-600, LC2-700 and LC2-700H, respectively. The deconvolution of the LC0-600 spectrum shows two major peaks at 398.7 and 400.7 eV, respectively, which correspond to pyridinic and pyridonic types of nitrogen. The calculation of the area ratio of the two deconvoluted peaks suggests there are about 64 at% pyridonic and 36 at% pyridinic nitrogen. The level of pyridinic nitrogen is greatly reduced to 9 at% after chemical activation at 700 °C and the binding energies of two peaks shift to 398.2 and 400.1 eV, respectively. The 400.7 to 400.1 eV peak shift may correspond to the transformation of pyridonic to pyrrolic types of nitrogen,[33] while the 398.7 to 398.2 eV peak shift may be due to the interaction between metal and pyridinic nitrogen, where electrons are transferred from metal to pyridinic nitrogen.[34]

More inorganic elements, including magnesium, calcium and phosphorus, appear in the XPS spectra after activation, because the activation reaction between KOH and carbon helps to etch through cell walls and expose what remain inside cells. In contrast, K, Na and Cl completely disappear because the samples are thoroughly washed by distilled water. Figure 3e and f are the high resolution Mg-1s and Ca-2p spectra of LC2-700. The magnesium spectrum shows a single peak at 1304.1 eV, indicating the magnesium element exists in the form of +2 ions. A similar conclusion can be drawn from the calcium spectrum, which indicates calcium exists in the form of +2 ions. It has been discussed in earlier studies that some residual potassium contents are detected after KOH chemical activation, even after the samples are washed.[25] Zhao et al. further proposed that the residual potassium may exist in the form of extra-framework cations.[13] In contrast, our XPS analysis does not detect residual potassium, which indicates both the intrinsic (from leaf cells) and extrinsic (from KOH) potassiums are not chemically grafted to the chemical structure of the resulting carbon samples. However, instead of potassium, magnesium and calcium are the residual metals in the resulting carbon structure. Furthermore, Table 2 shows all metal elements were washed away by 1M HCl acid (LC2-700H). In Figure 4, XRD analysis of all activated carbon samples have no diffraction peaks that are related to the crystal structures of magnesium and calcium or their corresponding metal oxides, which implies that those metal elements may not exist in those forms but are bonded with the resulting carbon structure in the form of cations.

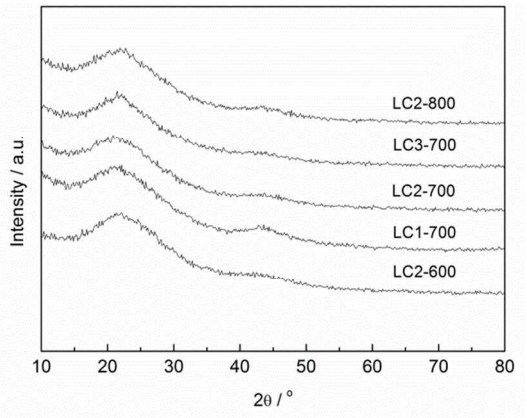

Figure 4 XRD diffraction pattern of leaf-derived carbon.

CO_2 Uptake of Leaf-derived Carbon

CO_2 adsorption tests were carried out from 0.01 to 1 bar CO_2 at 0 and 25 °C, respectively. The corresponding CO_2 adsorption isotherms and uptakes are plotted and summarised in Figure 5 and Table 3. LC2-700 shows the highest CO_2 uptakes of 19.4 wt% at 25 °C under 1 bar CO_2, while LC2-800 exhibits the

highest CO_2 uptake of 33.6 wt% at 0 °C. Besides materials mentioned in the introduction, the CO_2 adsorption capacity can also be compared with those of recently reported carbon sorbents under 1 bar and 25 °C, e.g., 12.5 wt% for dialdehyde and diamine derived microporous carbon,[35] 8.6 wt% for imine-linked polymer-derived carbon,[36] 13.6 wt% for polyimine-based carbon,[37] 15.0 wt% for fungi-based carbon.[38] Clearly, the London Plane leaf-derived carbon shows a superior capacity for CO_2 capture at identical conditions..

At 0 °C, all isotherms intersect with each other at different pressures below 0.7 bar. As the temperature increases to 25 °C, the upper bound of the intersection points rises to about 0.8 bar in Figure 5b. These changes of intersection points indicate an enhanced binding with CO_2 molecules at relatively lower pressures and higher temperatures. In addition, there is a 1.2 wt% difference between the CO_2 uptakes of LC2-700 and LC2-700H under 0.15 bar. This is a more significant difference in CO_2 uptake than that under 1 bar. It is mentioned in the porosity analysis that LC3-700 shows the highest specific surface area and LC2-800 possesses the highest ultramicropore volume, where these two porosity parameters are considered to have a significant influence on CO_2 uptake. However, both of those lead to relatively low CO_2 uptake at 25 °C. It implies that porosity is not the only factor that influences CO_2 uptake.

Table 3 Summary of CO_2 uptakes of leaf-derived carbon sorbents under 1 bar CO_2.

Sample	CO_2 uptake / wt%			
	1 bar		0.15 bar	
	0 °C	25 °C	0 °C	25 °C
LC1-700	27.9	18.0	12.4	6.8
LC2-700	30.4	19.4	11.2	6.2
LC2-700H	32.3	18.5	10.1	5.0
LC3-700	30.5	17.3	8.8	4.3
LC2-600	27.4	14.9	11.0	5.3
LC2-800	33.6	18.6	9.8	5.0

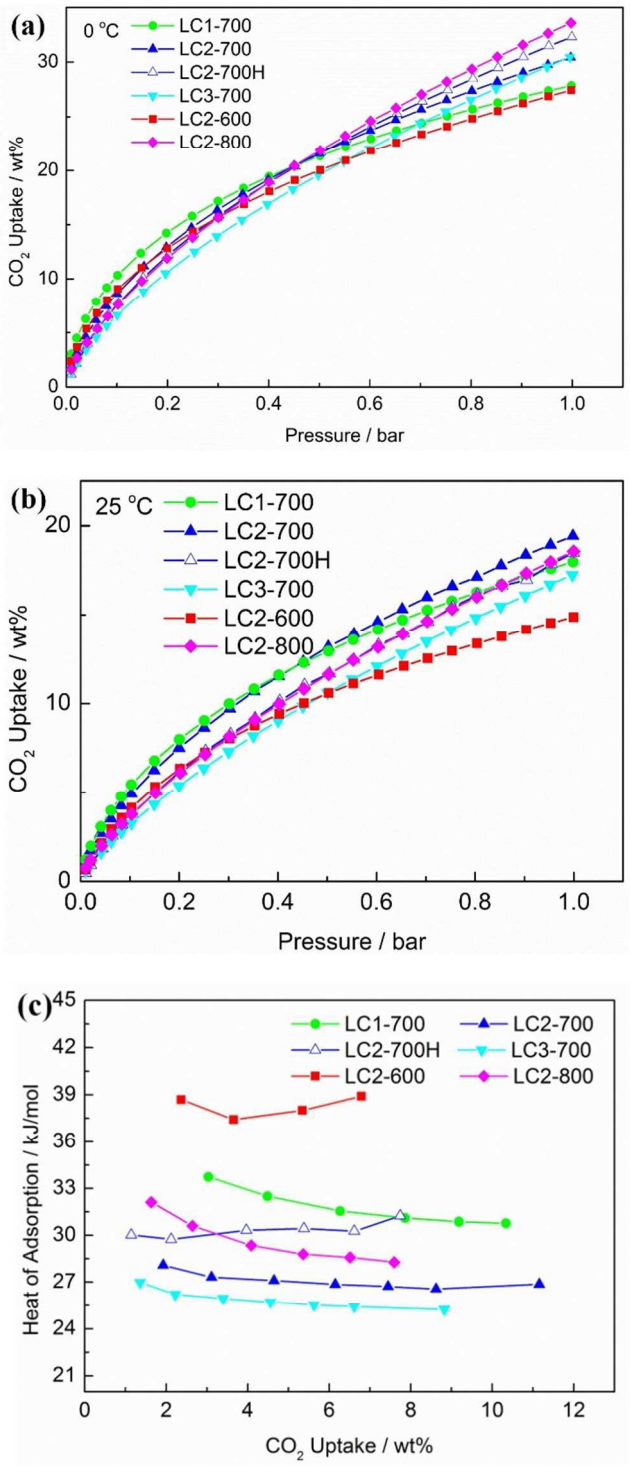

Figure 5 CO_2 adsorption isotherms of leaf-derived carbon sorbents at (a) 0 and (b) 25 °C from 0.1 to 1 bar and (c) their corresponding heats of adsorption.

It has been widely discussed in the literature that the presence of nitrogen in the sample enhances CO_2 binding with carbon sorbents due to its basic nature.[15, 16, 39-41] Both pyridinic and pyrrolic nitrogens exist in nitrogen-containing carbon sorbents, but the former is more influential due to its lone pair of electrons and thus exhibits higher basicity than the latter.[42] Small quantities of nitrogen are found in all activated samples, but the level of pyridinic nitrogen is further reduced with increasing KOH/carbon

weight ratio and activation temperature; correspondingly, its effect on CO_2 uptake also reduces. In addition to the nitrogen element, magnesium and calcium also exist in the samples. LC2-700 is the sample washed by distilled water while LC2-700H is washed by 1M HCl acid to remove the metal dopants. Figure 5a shows that the acid-washed sample LC2-700H exhibits a slightly higher CO_2 uptake than the water-washed counterpart at 0 °C under 1 bar, due to a slightly larger ultramicropore volume, as indicated in Table 1. However, LC2-700 shows a higher CO_2 uptake at 25 °C in Figure 5b instead. In addition, in Figure 5a, the LC2-700 and LC2-700H isotherms intersect with each other at about 0.5 bar, which indicates that LC2-700 even shows a higher CO_2 uptake than LC2-700H at the low pressure regime (<0.5 bar). At 25 °C, the isotherm of LC2-700H is entirely below that of LC2-700. It is previously mentioned that no crystalline metal or metal oxides are found by XRD analysis and the corresponding XPS suggests both Mg and Ca exist in the form of cations. In consideration of the previously referenced study on extra-framework cations,[13] magnesium and calcium may also be grafted to the carbon structures in a well dispersed form, as inherited from the leaf structure, and thus considerably enhance both the CO_2 binding through electrostatic interaction and the density of such active sites, leading to much increased CO_2 uptake.

Heat of Adsorption and Influence of Dopants

Figure 5b shows that there is an extra 0.9 wt% CO_2 uptake (under 1 bar CO_2 and 25 °C) in LC2-700 compared with LC2-700H. Under 0.15 bar and 25 °C, the difference is 1.2 wt%. It should be noted that LC2-700 possesses lower specific surface area, pore volume and ultramicropore volume than those of LC2-700H.

Figure 5c is the heat of adsorption plot of leaf-derived carbon. Differing from the CO_2 adsorption isotherm plots, LC2-600 shows higher heat of adsorption than those of all the other samples, while LC3-700 is at the bottom of the diagram. The heat of adsorption of a sample can be influenced by both its dopants and porosity. Considering LC2-600 shows the least developed porous structure, its high heat of adsorption can be solely attributed to dopants. However, LC2-600 possesses a considerable amount of both nitrogen and metal dopants. Therefore, it is difficult to distinguish their respective effects on the CO_2 uptake. It can be noted in Figure 5c that LC1-700 shows the second highest heat of adsorption and shows a less developed porous structure than LC2-700. It also contains a lower level of nitrogen but a higher level of calcium than LC2-700. Therefore, the higher heat of adsorption should be attributed to the existence of calcium dopants.

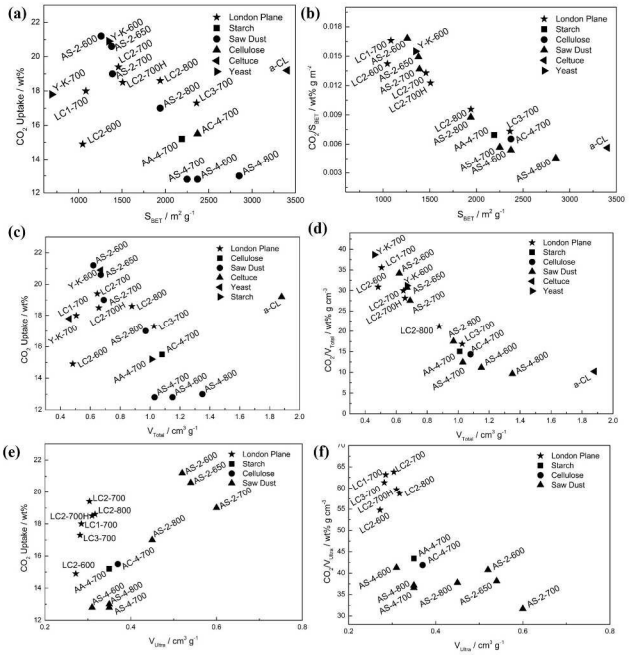

Figure 6: CO_2 uptake versus porosity parameters (a) BET surface area, (c) total pore volume and (e) ultramicropore volume; (b), (d) and (f) are their corresponding specific CO_2 uptake (CO_2 uptake/porosity) versus porosity parameter.

In addition, in Figure 6, CO_2 uptake and specific CO_2 uptake (CO_2 uptake/porosity) are plotted against their porosity parameters with both our experimental data and those referenced in the "Introduction" section of our manuscript, including starch, cellulose, sawdust, celtuce and yeast. It should be noted that specific BET surface area is used in this analysis, in order to be consistent with the characterisation data from the literature. The specific BET surface area of leaf-derived carbon is summarised in Table S1. It is noted from Figure 6a and c that higher specific surface area and pore volume do not necessarily play a dominant role in CO_2 adsorption. Those with higher specific surface area and pore volume do not necessarily have higher CO_2 uptakes. The same observation can be applied to Figure 6b and d. However, it is interesting to notice that our samples with higher metal contents (LC1-700 and LC2-600) changes from the bottom-left in Figure 6a and c to the top-left in Figure 6b and d. This change in positions suggests those two samples have higher CO_2 uptake per surface area and pore volume. Furthermore, Figure 6e shows those samples with ultramicropore volume also exhibit higher CO_2 uptake, such as the saw-dust derived carbon (on the top right of the figure). However, it can also be noticed that some samples with similar ultramicropore volume (on the left of the figure) shows different levels of CO_2 uptakes. In contrast to Figure 6e, all of our leaf-derived carbon samples occupy the top-left of Figure 6f, which indicates they have much higher CO_2 uptake per ultramicropore volume than those of the other samples. The common characteristics of these samples are the possession of nitrogen and metal dopants. This observation indicates that nitrogen and metal dopants play a more important role than porosity for the low pressure CO_2 capture (i.e. $\leqslant$ 1 bar).

Artificial neural network

An artificial neural network was built with Matlab R2013a to analyse the relationship between the influencing factors and CO_2 uptakes at 25 °C and under 1 bar CO_2. In this work, nitrogen, calcium, magnesium contents and ultramicropore volume were selected as input parameters, and the CO_2 uptakes at 25 °C and 1 bar CO_2 as the target parameter. In total, 31 experimental data pairs from this work and the literature were selected as the input data for building the network.[15,17,41,43,44] Within these experimental data pairs, 21 data pairs were used for training, while 5 for validation and 5 for testing. The training process was carried out by the "nftool" (neural network fitting toolbox) of Matlab by using the training function of "trainlm" (Levenberg-Marquardt backpropagation). After several trials, the network with 20 neurons and 1 hidden layer gave the best outcome with the R_{Train}=0.9404, $R_{Validation}$=0.9972 and R_{Test}=0.9154, respectively. Therefore, this network was chosen for the subsequent simulation.

After the network was trained, it was used to simulate the influences of input parameters on CO_2 uptakes. The simulation was carried out with the "nntool" (open network/data manager) of Matlab. Before the simulation, the following data processing was applied to the input parameters:

1. For each simulation, one of the four input parameters was set to be the variable, where its simulated data range was within the value range of its corresponding input parameter. The other three were set to be constant, where the value of a constant was the average of the maximum and minimum of input parameters. The corresponding values are summarised in Table 4.

Table 4 Summary of constants and variables for simulation.

Simulated Parameter	Max	Min	Average (Constant)	Input Data Range (Variable)
N content	6.7	0	3.4	0.3 – 6.0
Ca content	1.7	0	0.8	0.2 – 1.6
Mg content	0.9	0	0.4	0 – 0.60
Ultramicropore Volume	0.60	0.13	0.36	0.14 – 0.60

*For chemical content, the unit is "at%"; for ultramicropore volume, the unit is "cm^3/g".

2. For the chemical composition of each sample from the literature, its unit was converted into "at%" if necessary, while its value was recalculated into the composition of C, O, N, Ca and Mg, in order to be consistent with our own work. If an element was not detected in a sample in the literature, it was input as "0".

3. For both chemical composition and ultramicropore volume, if either of them (or both) was not reported for a sample in the literature, it is input as "NaN" (Not a Number).

The simulated output data were then plotted in Figure 7. It is clearly observed from Figure 7 that the CO_2 uptake increases rapidly with the increasing calcium, magnesium contents and ultramicropore volume. However, the CO_2 uptake does not vary regularly with increasing nitrogen content. These predicted influences of input parameters on CO_2 uptake are consistent with the analysis in the previous chapter, which emphasises that metal dopant and ultramicropore are the two key determinants for CO_2 capture performance of porous carbon materials. The irregular change of CO_2 uptake with nitrogen content can be explained by the existence of various nitrogen functional groups. It is mentioned in the previous chapter that nitrogen dopant can exist in different forms, such as pyridinic and pyrrolic nitrogen. The former has a higher affinity towards acidic CO_2 molecules due to its higher basicity. The composition of different forms of nitrogen is not frequently reported in the literature. Therefore, it is difficult to distinguish their individual influences on CO_2 capture. Furthermore, it is also observed from Figure 7 that the Mg content curve is slightly steeper than that of Ca content. This suggests that Mg dopant may have a greater influence than that of Ca dopant on CO_2 uptake according to the prediction. It shows that this network can help to distinguish the contribution of different metal dopants on CO_2 uptake.

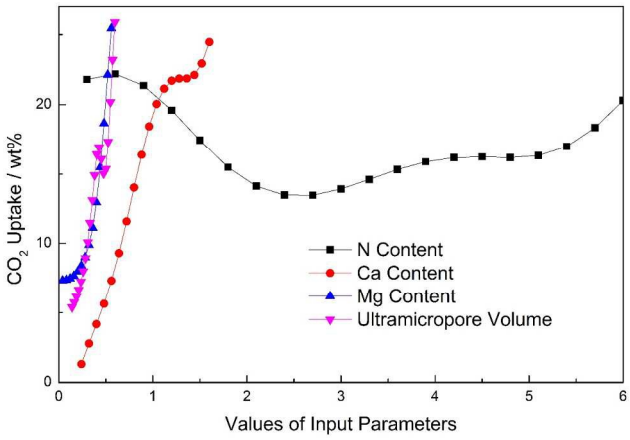

Figure 7 The predicted influence of input parameters on CO_2 uptake

Oxygen Reduction Catalytic Activity of Leaf-derived Carbon

The electrochemical performance of leaf-derived carbon materials is investigated by the rotating disk electrode (RDE) voltammetry. The measurement is conducted in oxygen-saturated 0.1M KOH electrolyte, with Ag/AgCl (sat. KCl) as reference electrode. The current density shown here is determined by the measured current divided by the geometric surface area of the glassy carbon (GC) working electrode. Figure 8 shows the linear sweep voltammetry (LSV) of the leaf-derived carbon at 1600 RPM. It is clear the electrochemical activities of all lead-derived carbon samples are much more significant than the GC background, confirming the occurrence of catalytic oxygen reduction. It is also noted that the catalytic activity of LC2-700 outperforms the rest of water-washed leaf-derived carbon, and the electrochemical performance of acid-washed LC2-700H (washed by HCl) is even better than that of LC2-700, both in terms of the

onset/half-wave reduction potential and the measured current density at a given potential. The LC2-600 sample shows the most negative onset/half-wave reduction potential, which is probably because the lower activation temperature (600 °C) leads to incomplete carbonisation (much lower carbon and higher oxygen ratio from XPS, Table 2) and thus a lack of electrical conductivity. Cyclic voltammetry measurement of the carbon (Figure S4) also supports this argument. The LSV plots of LC3-700 and LC2-800 are similar, while the LC1-700 shows a slightly more positive onset potential, but with a much broader reduction potential range before the diffusion limiting current is achieved. This is because the LC3-700 and LC2-800 possess larger surface areas but with much lower nitrogen contents, whereas the LC1-700 shows a higher nitrogen content but much lower surface area. Such a phenomenon will be further explained by the Tafel plots measurement later (Figure 10). In this regard, the catalytic activities of LC2-700 and LC2-700H are better than the rest due to a combination of relative large surface area and the highest nitrogen content among all the leaf-derived carbon.

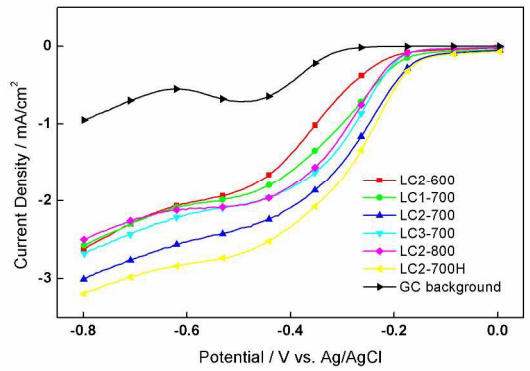

Figure 8 Linear sweep voltammetry of leaf-derived carbon and barely glass carbon (GC) tip background in 0.1M KOH at 1600 RPM.

The ORR catalytic activities of the leaf-derived carbons are further investigated by the number of electron exchange during the reaction, based on the Koutecky-Levich equation:

$$1/J = 1/J_L + 1/J_k = 1/0.62nFC_0(D_0)^{2/3}v^{-1/6}\omega^{1/2} + 1/J_k$$

where J is the measured current density (mA/cm^2), J_L and J_k are the diffusion-limiting and kinetic current densities (mA/cm^2) respectively, n is the overall number of electron transferred in the oxygen reduction, F is Faraday constant (96483 sA/mol), C_0 is the bulk saturated concentration of O_2 in 0.1 M KOH (1.2×10^{-3} mol/L), D_0 is the diffusion coefficient of O_2 in 0.1 M KOH (1.9×10^{-5} mol/L), ν is the kinematic viscosity of the 0.1 M KOH (0.01 m^2/s), and ω is angular velocity of the disk (rad/s)[45]. According to the Koutecky-Levich plots (K-L plots, 1/J vs. $\omega^{1/2}$, Figure 9a), the number of electron exchange during ORR can be calculated from the slope, $1/0.62nFC_0(D_0)^{2/3}v^{-1/6}$. It is seen from the Table 5 and Figure S5 that the electron transfer number of LC2-700 at -0.6 V vs. Ag/AgCl is 3.04, higher than those of all the other water-washed leaf-derived carbon samples. The value of electron transfer number for LC2-700 (3.04) suggests a combined two-electron and four-electron pathway, partly because the majority of nitrogen species is pyrrolic (Figure 3c) and is not the most reactive in terms of catalysis for ORR. In addition to nitrogen doping, metal also plays a role in the ORR activity of leaf derived carbon. It is shown in Figure 9b the number of electron transfer for acid-washed LC2-700H is much higher than that of water-washed LC2-700 over a broad range of potential from -0.4 to -0.6 V vs. Ag/AgCl. The electron transfer number for LC2-700H at -0.6V is 3.73, very close to 4, indicating a near four-electron reduction pathway. Given the very similar microporous structures of LC2-700 and LC2-700H (Table 1), such an enhancement should be attributed to the removal of metal species after acid washing. In this case, metal dopants such as Ca and Mg are not the active sites for the catalytic reaction and act as 'dead mass'.

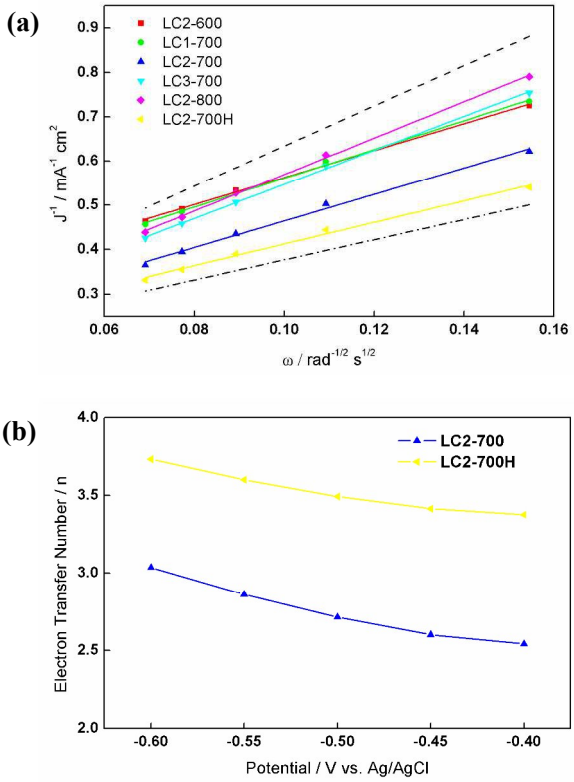

Figure 9 (a) Koutecky-Levich plots for leaf derived carbon at -0.6 V vs. Ag/AgCl, calculated based on the LSV results; (b) electron transfer number for LC2-700 and LC2-700H in the potential range of -0.4 to -0.6 V vs. Ag/AgCl.

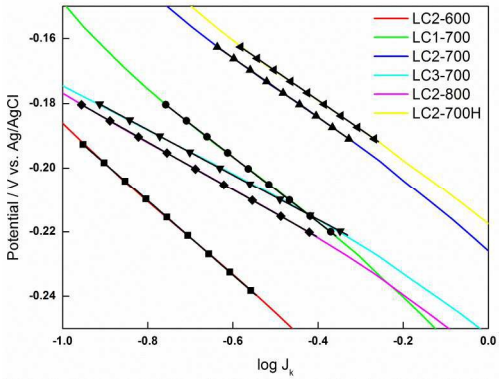

Figure 10 Tafel plots of leaf derived carbon between the potential -0.15 to -0.25 V vs. Ag/AgCl (rotation speed is 1600RPM.

Table 5 Number of electron Transfer for leaf derived carbon at -0.6 V vs. Ag/AgCl.

Sample	LC2-600	LC1-700	LC2-700	LC2-700H	LC3-700	LC2-800
n	2.98	2.79	3.04	3.73	2.36	2.20

Tafel plots of leaf derived carbon samples are further applied to characterise the reduction kinetics. As show in Figure 10, within the potential range of -0.15 to -0.25 V vs Ag/AgCl (the fast reduction range), the LC2-700H sample shows the highest kinetic current density, followed by LC2-700. However the Tafel slopes of LC2-700H and LC2-700 (90.2 and 92 mV/dec, respectively) are greater than that of LC3-700 and LC2-800 (69.8 and 75.5 mV/dec, respectively). One possible reason is the higher specific surface area (Table 1) for LC3-700 and LC2-800 leads to potentially easy access to those active sites and thus smaller Tafel plot at low potential range. However the real amount of exposed active sites is determined by the nitrogen content (Table 2), which is very low for these two samples, leading to overall sluggish reduction kinetics – smaller kinetic current density (Figure 10) and smaller electron transfer number (Table 5). Contrary to that, the LC1-700 shows a larger Tafel plot (102.4 mV/dec) and a greater level of electron transfer than LC3-700 and LC2-800, as it possess higher nitrogen content but smaller specific surface area. The small kinetic current density and large Tafel plot (115.7 mV/dec) of LC2-600 is explained by the lack of carbonisation, as discussed before.

Conclusions

London Plane leaf waste, rich in lignocelluloses with a cellular structure, is an ideal precursor for the production of low-cost but high-performance microporous carbon materials. The KOH/carbon weight ratio and activation temperature are the two major factors that largely influences the final porous structure and chemical composition of the resulting materials. Equally important are the biological structure and chemistry of the leaves, particularly well dispersed nitrogen, magnesium and calcium dopants in the derived carbon. Activated at 700 °C and with a KOH/carbon weight ratio 2:1, washed by distilled water, the sample shows the highest CO_2 uptake of 19.4 wt% under 1 bar CO_2 and 25 °C, as a result of the highly developed microporous structure and the preservation of nitrogen and elemental metal contents doped in the carbon materials. The dopants exist in the form of aromatic nitrogen and metal cations, respectively, which can enhance CO_2 binding on carbon by means of Lewis basicity and electrostatic interactions. The positive influence of metal dopants on CO_2 uptake is further demonstrated by the artificial neural network analysis. Those samples with nitrogen and metal dopants show higher CO_2 uptake per unit porosity. However, in contrast, the sample with the best ORR catalytic performance is prepared under the same activation condition but after being washed by 1M HCl to remove the metal contents, because the metal contents play the role of "dead mass" in ORR with little contribution to the catalysis of the reaction. The highly porous LC2-700H with specific surface area 1630 m^2/g shows an almost direct four-electron pathway, despite the nitrogen bonding configuration is mostly in the pyrrolic form. To summarise, here we present a facile synthesis of highly microporous carbon, derived from "zero-cost" London Plane leaf wastes, which has shown excellent potential in CO2 capture and ORR catalysis. The optimal performance in both applications is determined by the combined effect of the highly developed microporous structure plus the intrinsic nitrogen and metal doping. Appropriate preparation procedures have been carefully devised for the two different types of applications.

Acknowledgements

The authors would like to acknowledge the financial support from the UK EPSRC (EP/G063176/1, EP/G061785/1, and EP/I010955/1) and research support was gratefully received from the Department of Chemistry, University College London.

Notes

[a] *Department of Chemistry, University College London, 20 Gordon Street, London WC1H 0AJ, United Kingdom; email: z.x.guo@ucl.ac.uk*
[b] *School of Environmental Sciences, University of East Anglia, Norwich NR4 7TJ, United Kingdom; email: c.shang@uea.ac.uk*

† Electronic Supplementary Information (ESI) available: [details of any supplementary information available should be included here]. See DOI: 10.1039/b000000x/

References

1. D. M. D'Alessandro, B. Smit and J. R. Long, *Angew. Chem. Int. Ed.*, 2010, **49**, 6058-6082.
2. T. C. Drage, C. E. Snape, L. A. Stevens, J. Wood, J. Wang, A. I. Cooper, R. Dawson, X. Guo, C. Satterley and R. Irons, *J. Mater. Chem.*, 2012, **22**, 2815-2823.
3. S. L. Candelaria, Y. Y. Shao, W. Zhou, X. L. Li, J. Xiao, J. G. Zhang, Y. Wang, J. Liu, J. H. Li and G. Z. Cao, *Nano Energy*, 2012, **1**, 195-220.
4. L. M. Dai, D. W. Chang, J. B. Baek and W. Lu, *Small*, 2012, **8**, 1130-1166.
5. Y. P. Zhai, Y. Q. Dou, D. Y. Zhao, P. F. Fulvio, R. T. Mayes and S. Dai, *Adv. Mater,.* 2011, **23**, 4828-4850.
6. K. Gong, F. Du, Z. Xia, M. Durstock and L. Dai, *Science*, 2009, **323**, 760-764.
7. L. Yang, S. Jiang, Y. Zhao, L. Zhu, S. Chen, X. Wang, Q. Wu, J. Ma, Y. Ma and Z. Hu, *Angew. Chem. Int. Ed.*, 2011, **50**, 7132-7135.
8. M. Lefèvre, E. Proietti, F. Jaouen and J.-P. Dodelet, *Science*, 2009, **324**, 71-74.
9. Y. Y. Liang, Y. G. Li, H. L. Wang, J. G. Zhou, J. Wang, T. Regier and H. J. Dai, *Nature Materials*, 2011, **10**, 780-786.
10. Y. Liang, Y. Li, H. Wang and H. Dai, *J. Am. Chem. Soc.*, **135**, 2013-2036.
11. H. Wang and H. Dai, *Chem. Soc. Rev.*, **42**, 3088-3113.
12. G. Zhang, B. Y. Xia, X. Wang and X. W. Lou, *Adv. Mater., DOI: 10.1002/adma.201304683*.
13. Y. Zhao, X. Liu, K. X. Yao, L. Zhao and Y. Han, *Chem. Mater.*, 2012, **24**, 4725-4734.
14. C. Cazorla, S. A. Shevlin and Z. X. Guo, *J. Phys. Chem. C*, 2011, **115**, 10990-10995.
15. M. Sevilla, P. Valle-Vigón and A. B. Fuertes, *Adv. Funct.*

Mater., 2011, **21**, 2781-2787.
16. B. Zhu, K. Li, J. Liu, H. Liu, C. Sun, C. E. Snape and Z. Guo, *J. Mater. Chem. A*, 2014, **2**, 5481-5489.
17. M. Sevilla and A. B. Fuertes, *Energ. & Environ. Sci.*, 2011, **4**, 1765-1771.
18. R. Wang, P. Wang, X. Yan, J. Lang, C. Peng and Q. Xue, *ACS Appl. Mater. Interfaces*, 2012, **4**, 5800-5806.
19. S. Gao, H. Fan, Y. Chen, L. Li, Y. Bando and D. Golberg, *Nano Energy*, 2013, **2**, 1261-1270.
20. H. Zhu, J. Yin, X. L. Wang, H. Y. Wang and X. R. Yang, *Adv. Funct. Mater.*, 2013, **23**, 1305-1312.
21. London plane Platanus x hispanica, http://apps.kew.org/trees/?page_id=119, 2014.
22. NIST XPS Database, http://srdata.nist.gov/xps/ElmComposition.aspx.
23. H. Daun, in *Produce Degradation: Pathways and Prevention*, ed. O. Lamikanra and S. H. Imam, Taylor & Francis, Boca Raton, 2005, pp. 200.
24. M. Roberts, M. J. Reiss and G. Monger, in *Advanced Biology*, Nelson, Cheltenham, 2000, pp. 15&203.
25. A.N. A. El-Hendawy, *Appl. Surf. Sci.,* 2009, **255**, 3723-3730.
26. J. Wang and S. Kaskel, *J. Mater. Chem.*, 2012, **22**, 23710-23725.
27. J. Romanos, M. Beckner, T. Rash, L. Firlej, B. Kuchta, P. Yu, G. Suppes, C. Wexler and P. Pfeifer, *Nanotechnology*, 2012, **23**, 015401.
28. C. Starr, R. Taggart, C. Evers and L. Starr, in *Volume 4 - Plant Structure & Function (Biology the Unity & Diversity of Life)*, Cengage Learning, Belmont, 2012, pp. 461.
29. M. Riederer and L. Schreiber, *J. Exp. Bot.*, 2001, **52**, 2023-2032.
30. P. van der Heide, in *X-Ray Photoelectron Spectroscopy*, John Wiley & Sons, Inc., Hoboken, 2011, pp. 1-12.
31. P. S. Nobel, in *Physicochemical and Environmental Plant Physiology*, Elsevier, Oxford, 4th edn., 2009, pp. 32.
32. H. Im, F. Rasouli and M. Hajaligol, *J. Agric. Food Chem.*, 2003, **51**, 7366-7372.
33. J. R. Pels, F. Kapteijn, J. A. Moulijn, Q. Zhu and K. M. Thomas, *Carbon*, 1995, **33**, 1641-1653.
34. G. Wu, Z. Chen, K. Artyushkova, F. H. Garzon and P. Zelenay, in *Proton Exchange Membrane Fuel Cells 8: ECS Transactions: Volume 16, Issue 2*, ed. T. Fuller, The Electrochemical Society, Pennington, 2008, pp. 166.
35. J. Wang, Q. Liu, *Nanoscale*, 2014, **6**, 4148
36. J. Wang, I. SenKovska, M. Oschatz, M. R. Lohe, L. Borchardt, A. Heerwig, Q. Liu, S. Kaskel, *ACS Appl. Mater. Interfaces* 2013, **5**, 3160
37. J. Wang, I. SenKovska, M. Oschatz, M. R. Lohe, L. Borchardt, A. Heerwig, Q. Liu, S. Kaskel, *J. Mater. Chem. A*, 2013,**1**, 10951-10961
38. J. Wang, A. Heerwig, M. Oschatz, M. R. Lohe, L. Borchardt, S. Kaskel, *J. Mater. Chem.*, 2012, **22**, 13911
39. Y. Zhao, L. Zhao, K. X. Yao, Y. Yang, Q. Zhang and Y. Han, *J. Mater. Chem.*, **22**, 19726-19731.
40. C. Chen, J. Kim and W.-S. Ahn, *Fuel*, **95**, 360-364.
41. L. Liu, Q.-F. Deng, X.-X. Hou and Z.-Y. Yuan, *J. Mater. Chem.*, 2012, **22**, 15540-15548.
42. J. Miyawa and S. Schulman, in *Handbook of Pharmaceutical Analysis*, ed. L. Ohannesian and A. Streeter, Taylor & Francis, New York, 2001, pp. 200-201.
43. W. Hao, E. Bjorkman, M. Lilliestrale, and N. Hedin, *Appl. Energ.*, 2013, **112**, 526-532.
44. K. C. Kemp, V. Chandra, M. Saleh, and K. S. Kim, *Nanotechnology*, 2013, **24**, 235703.
45. K. Qiu and Z. X. Guo, *J. Mater. Chem. A*, 2014, **2**, 3209-3215.

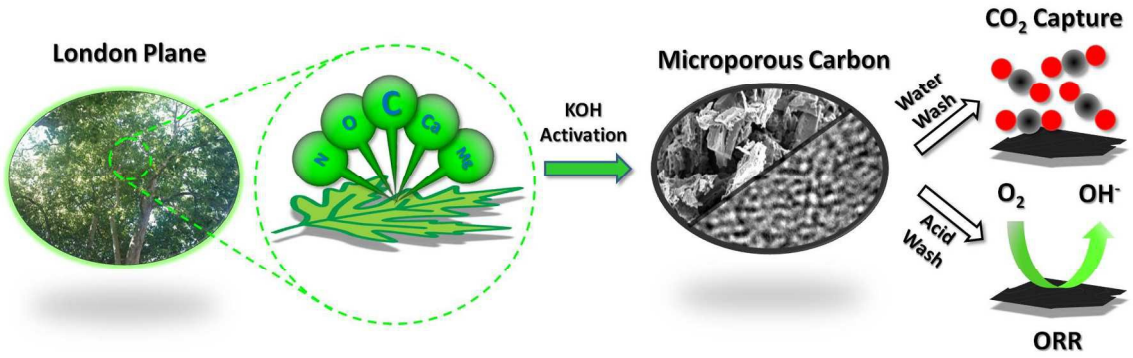

A low-cost high-performance "green carbon", derived from London Plane leaves, exhibits excellent sorption capacity for CO_2 capture and electro-catalytic capability for oxygen reduction, due to naturally doped nitrogen and metallic elements inherited from the biomass.